

Dynamical Properties of Merging Galaxy Clusters from Simulated Analogs

DAVID WITTMAN¹

¹*Physics Department, University of California, Davis, CA 95616*

ABSTRACT

Merging galaxy clusters may provide a unique window into the behavior of dark matter and the evolution of member galaxies. To interpret these natural collider experiments we must account for how much time has passed since pericenter passage (TSP), the maximum relative speed of the merging subclusters, merger phase (outbound after first pericenter or returning for second pericenter), and other dynamical parameters that are not directly observable. These quantities are often inferred from staged simulations or analytical timing arguments that include neither substructure, large-scale structure, nor a cosmologically motivated range of impact parameters. We include all these effects by extracting dynamical parameters from analog systems in a cosmological n-body simulation, and we present constraints for 11 observed systems. The TSP and viewing angles we derive are consistent with those of staged hydrodynamical simulations, but we find lower maximum speeds. Compared to the analytical MCMAC method we find lower TSP, and viewing angles that put the separation vector closer to the plane of the sky; we attribute this to the MCMAC assumption of zero pericenter distance. We discuss potential extensions to the basic analog method as well as complementarities between methods.

Keywords: galaxies: clusters: general

1. INTRODUCTION

The merger of two clusters of galaxies triggers a range of astrophysical processes. Shocks in the intracluster medium launched around the time of pericenter trigger synchrotron emission (detectable as radio “relics”: [Ensslin et al. 1998](#); [Feretti et al. 2012](#); [Skillman et al. 2013](#)), accelerate cosmic rays ([Brunetti & Jones 2014](#)), and may affect star formation and AGN activity ([Miller & Owen 2003](#); [Sobral et al. 2015](#)). X-ray morphology is also greatly affected as gas associated with each cluster can be stripped or displaced around the time of pericenter. Mergers also place upper limits on momentum exchange between dark matter particles ([Markevitch et al. 2004](#); [Randall et al. 2008](#); [Kahlhoefer et al. 2014](#); [Robertson et al. 2017](#); [Wittman et al. 2018b](#); [Harvey et al. 2018](#)). Any galaxy-dark matter displacement created at pericenter crossing can, however, change sign later as the galaxies in each subcluster fall back to, and through, the center of their host dark matter halo ([Kim et al. 2017](#)). Hence the interpretation of an observed state hinges on knowing the merger phase (outbound toward

first apocenter or returning toward second pericenter) and more specifically the time since pericenter (TSP). Merger effects on star formation must be interpreted in the same light. The claims that some mergers have stimulated star formation ([Miller & Owen 2003](#); [Ma et al. 2010](#); [Sobral et al. 2015](#); [Stroe et al. 2017](#)), some have quenched it ([Mansheim et al. 2017](#)), and some have had no effect ([Chung et al. 2010](#)) may not conflict given that each system is seen at a different TSP. It is also possible that pericenter speed has an effect with low speeds compressing, but high speeds disrupting, star-forming gas. A coherent picture can emerge only if we have access to robust methods of inferring the dynamics of each system from the one snapshot we observe.

Efforts to do this date back to the timing argument of [Kahn & Woltjer \(1959\)](#), which uses equations of motion for two point masses on radial trajectories in an expanding universe. Given the observed masses, separation, and relative speed, the timing argument can reveal the time since pericenter and speed at the time of pericenter. Observations, however, reveal only the projected separation and line-of-sight component of the relative velocity vector. This motivated [Dawson \(2013\)](#)

to update the timing argument with a code, MCMAC,¹ that marginalizes over possible viewing angles, along with other improvements such as using Navarro-Frenk-White (Navarro et al. 1997) mass profiles rather than point masses. He showed that uncertainty in viewing angle is a substantial source of uncertainty in dynamical parameters such as time since pericenter (TSP) and the maximum speed v_{\max} .

Wittman et al. (2018a, hereafter WCN18) constrained the viewing angle of observed clusters by “observing” analogs in the MultiDark cosmological n-body simulation. This work improved the viewing angle constraints as follows. Because MCMAC assumes radial orbits, the velocity vector is always parallel to the separation vector; thus any nonzero observed line-of-sight velocity difference between subclusters, $|\Delta v_{\text{los}}| > 0$, rules out the possibility of the separation vector being in the plane of the sky. This constraint is noteworthy because in its absence spherical geometry would dictate that the sky plane is the *most* likely orientation for a random vector. WCN18 showed that in mergers drawn from cosmological n-body simulations the velocity vector does have some component perpendicular to the separation vector, so that the plane-of-sky configuration remains quite likely for $|\Delta v_{\text{los}}|$ up to several hundred km/s. Most observed systems have $|\Delta v_{\text{los}}|$ in this range (Golovich et al. 2018). Indeed, WCN18 found that for most of the systems they considered, the likelihood of the viewing angle (defined as the angle between the line of sight and the separation vector) is a monotonically rising function that peaks at 90° , whereas MCMAC typically produced a rise followed by a sharp cutoff from $\approx 80 - 90^\circ$. The two methods did agree that observed systems with large $|\Delta v_{\text{los}}|$ ($\gtrsim 1000$ km/s) have separation vectors $\sim 45^\circ$ from the line of sight; in other words, a substantial fraction of a subcluster’s plunging motion must be along the line of sight to make $|\Delta v_{\text{los}}|$ this large.

In this paper we extend the analog method to infer the dynamical quantities of most interest, TSP and v_{\max} . We also show that for some observed systems analogs can reveal the phase of the orbit, i.e. whether the subclusters are outbound after first pericenter or returning after first turnaround.

The remainder of the paper is organized as follows. In §2 we outline our method, and in §3 we show results for nine merging systems with a range of properties. In §4 we compare our procedure with MCMAC by finding analogs of the two systems analyzed by Dawson (2013), and in §5 we summarize and discuss the im-

plications. To maintain consistency with the simulation described below, we adopt the flat Planck Collaboration et al. (2014) cosmology, in which $H_0 = 67.8$ km/s/Mpc and $\Omega_m = 0.307$.

2. METHOD

As in WCN18, we used the publicly available Big Multidark Planck (BigMDPL) Simulation (Klypin et al. 2016) hosted on the *cosmosim.org* website. BigMDPL has a box size of $(2.5 \text{ Gpc/h})^3$ and a particle mass of $2.359 \times 10^{10} M_\odot$, yielding at least 2500 particles for all halos in the mass range we consider. The database includes a halo catalog created by the Rockstar algorithm (Behroozi et al. 2013), from which we extract all halos with virial masses $> 6 \times 10^{13} M_\odot$. We then find pairs of halos separated by ≤ 5 Mpc, excluding pairs for which either member is within 5 Mpc of a third halo. This is to mimic the selection of observed binary clusters; the method could be extended to select analogs of more complicated mergers but this is beyond the scope of this paper. Having done this separately for all snapshots, we then match pairs across snapshots to obtain a history for each pair and, as in WCN18, discarded pairs that were never separated by < 300 kpc in any snapshot as well as pairs with multiple pericenters closer than this. This is because the real clusters for which we seek analogs have stripped X-ray morphologies that strongly suggest a recent first pericenter with a small pericenter distance.

We selected one halo from each pair to serve as a reference, and recorded the separation and velocity vectors at each snapshot. This improves on the method of WCN18, who recorded only the magnitude of the separation at each snapshot, as follows. Unlike WCN18 we are concerned with the time evolution and wish to interpolate between snapshots. The cartesian components of the halo separation vector vary smoothly through pericenter while the magnitude does not, as shown in the top panel of Figure 1. Hence we interpolate the components onto a finer time grid and use these interpolated components to reconstruct the magnitude of the separation. The top panel shows that linear interpolation of the magnitude overestimates the pericenter distance, and better performance is provided by either linear or cubic spline interpolation of the components. The bottom panel shows that when there are gaps, cubic spline is a better way to interpolate the components. We also tried cubic spline interpolation of the magnitude, but this caused unphysical ringing.

In a few trajectories, the halo separation recorded in the BigMDPL database appears not to be a smooth function of snapshot number. This may be due to accretion of smaller halos or perhaps to artifacts of assigning

¹ <https://github.com/MCTwo/MCMAC>

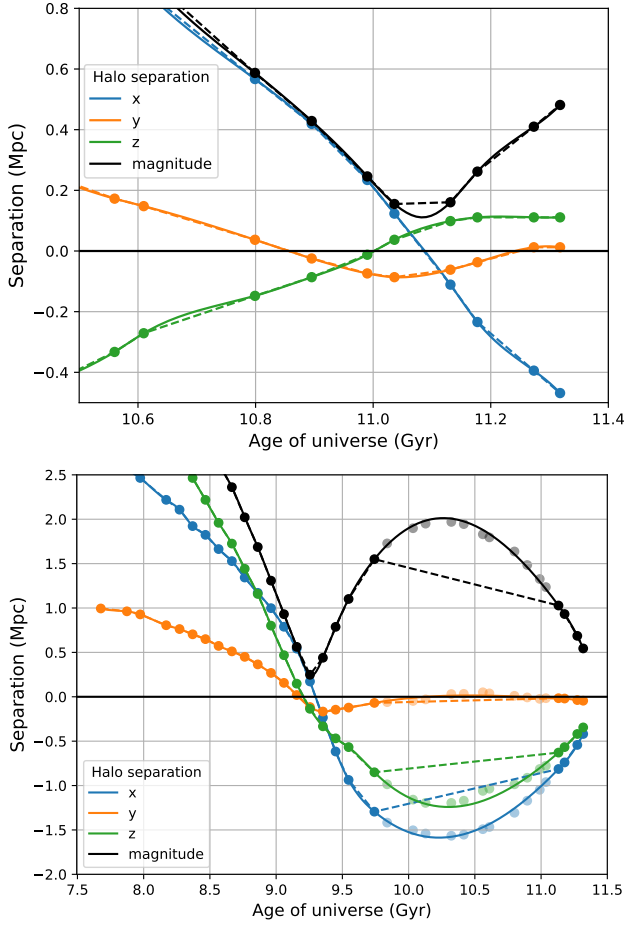


Figure 1. Interpolation performance: markers indicate halo separations recorded at the snapshots, with dashed (solid) curves indicating linear (cubic spline) interpolation. *Top:* linear interpolation of the separation magnitude (dashed black line) overestimates pericenter distance, so we use the magnitude of the interpolated values of the more smoothly varying cartesian components (black curve). This works well regardless of the type of interpolation used for the components. *Bottom:* the interpolation type matters when there are gaps in the halo catalog time series. Here, translucent points withheld to simulate such a gap demonstrate the accuracy of the cubic spline interpolation.

particles to halos. In these cases the interpolation causes a small amount of ringing evident as ripples in a few of the trajectories presented below. This does not substantially affect the inference of TSP or pericenter distance, because the ripples are small and because they occur in a small fraction of trajectories. We retain the cubic spline interpolation in spite of these occasional ripples because it works across gaps (Figure 1, bottom panel). This is not strictly necessary for this paper, which deals only with the times of observation and of pericenter, but it potentially enables interpolation of apocenter distances and periods.

In about 5% of the trajectories, the halo catalogs had swapped the halo identification numbers at some point near pericenter; this was evident by the sudden reversal of sign of all relative position and velocity components. This leaves a false impression that each component passed through zero between snapshots, but it does not change the separation magnitude at the snapshots. Hence, linear interpolation of the separation magnitude is more robust in these cases. We were able to detect and undo most of the halo swaps in an automated way by triggering on the change in the velocity vector from one snapshot to the next; halo swaps make this quantity unphysically large. Nevertheless, there were still some cases (often involving multiple halo swaps) where an attempted unswapping did not overwhelmingly improve this metric, and in these cases ($\approx 2\%$ of the total) we fell back to the less precise but more robust interpolation of the separation magnitude.

BigMDPL snapshots are typically separated by redshift increments of about 0.01, or time increments of about 100 Myr, so our interpolation typically yields TSP accurate to ≈ 10 Myr. This is a small fraction of the typical cluster TSP of ≈ 400 Myr. At some redshifts, however, BigMDPL leaves a larger (≈ 0.04) redshift gaps between snapshots. In the few cases where an observed cluster fell at one of these redshifts, we “observed” the analogs at a slightly higher redshift so the preceding trajectory would be well sampled.

This procedure gives good resolution for TSP and pericenter distance, but the velocity history is not so easily interpolated. We found that the halo catalogs often recorded a drop in relative velocity around the time of pericenter; Figure 2 shows an extreme example. This is presumably an artifact of identifying which particles belong to which halo. (Such artifacts may exist in the halo positions as well, but the separation at this time is so small that the absolute bias in separation cannot be large; in contrast, the velocity should be maximum here so the bias is notable.) Because the cataloged speed at the time of pericenter could be a substantial underestimate, we tabulate v_{\max} , the maximum cataloged speed, which typically occurs before pericenter. This is still a slight underestimate of the pericenter speed: a linear extrapolation² of the rising speed to the time of pericenter typically yields 100–200 km/s additional speed.

The probability of an analog matching the observed masses, d_{proj} , and Δv_{los} at a given polar viewing angle θ is calculated as in WCN18. Note that this calculation is unaffected by any halo swap, as it depends only on

² The speed is rising approximately linearly with time because these are extended halos, not point masses.

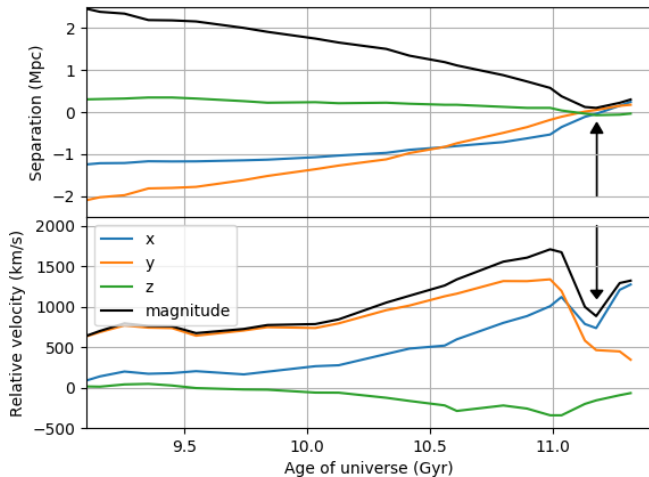


Figure 2. An extreme example of the drop in the halo relative velocity (lower panel) before the separation (upper panel) reaches a minimum (at the time indicated by the arrows). The components of each vector are shown in color and the magnitude in black. This drop in speed is likely an artifact due to difficulty in assigning particles to halos. Therefore, we record the maximum speed rather than the speed at the time of pericenter.

the “observed” snapshot rather than the time evolution. We rewrote the WCN18 code for this and most other steps to be more efficient, and we verified that both codes deliver the same result on common outputs such as the probability as a function of viewing angle. Here, however, we integrate over the viewing angle to assign an overall probability to each analog. This probability is then used to weight the TSP of that analog when inferring TSP, and similarly with the other dynamical parameters.

Parameter recovery tests. We present a series of tests using BigMDPL systems as “observed” systems where the true values of the parameters are known. We use systems from snapshot 74 (corresponding to redshift 0.1058) and assign the observational uncertainties listed for the observed cluster ZwCl 0008.8+5215 below. In each case we remove the “observed” system from the BigMDPL catalog, run the analog-finding code, and compare the results to the true values for the system.

For each system we infer TSP, v_{\max} , viewing angle θ (with the convention that $\theta = 90^\circ$ corresponds to a separation vector in the plane of the sky), and the angle φ between the separation vector and the velocity vector of the analog. This serves as a proxy for outbound vs. returning phases of the merger: $\varphi = 0$ indicates radially outbound, $\varphi = 180^\circ$ indicates radially inbound, and nonradial trajectories will shift from $\varphi < 90^\circ$ to $\varphi > 90^\circ$ at apocenter. We do not attempt to infer the pericenter distance because we found a similar broad range of peri-

center distances regardless of the specific values of d_{proj} and Δv_{los} used to winnow the analogs. It is possible that other observables such as X-ray morphology could constrain the pericenter distance if the analog method were to be extended to hydrodynamic simulations.

We begin with System A, whose distinguishing feature is a low 3-D velocity at the time of observation ($v_{3D}(t_{\text{obs}}) = 534$ km/s, in the bottom 2% of systems in snapshot 74) which will make Δv_{los} change little with viewing angle. This is coupled to a large TSP (802 Myr, in the top 10% of systems identified in snapshot 74). With a separation vector of (0.574, 0.210, -0.818) Mpc and a velocity vector of (376, 164, -342) km/s, placing the line of sight along the y axis yields $\Delta v_{\text{los}} = 164$ km/s and $d_{\text{proj}} = 0.999$ Mpc, typical of observed systems considered in this paper.

Figure 3 shows the cumulative distribution functions (CDFs) for the inferred parameters using the default set of analogs (blue curves) and a restricted set with small (< 150 kpc) pericenter distance (orange curves). The two sets of curves are quite similar, indicating that these parameters can be inferred without knowledge of the pericenter distance. We further tested the effects of this cut on other simulated systems, with consistently negligible effects. We therefore focus on the blue set of curves in the following comments on Figure 3, and retain the 300 kpc cut for the remainder of this section. The following section will show that results for real observed systems are also insensitive to this cut.

The shaded regions in Figure 3 mark the 68% highest probability density confidence intervals (HPDCI). In other words, each blue curve exits this region 0.68 higher than it entered, and the region shown is the most compact contiguous region meeting this criterion. In each panel, the true value (gray line) is within the 68% HPDCI, and also near the median analog value (where the curve crosses 0.5). This shows that the inference procedure works well, at least for this merging system and this line of sight.

We now examine how the constraints may vary with the viewing geometry. Table 1 lists the basis vectors for five lines of sight (LOS) for System A. LOS 2 is the one already examined above, while the others explore a range of d_{proj} and Δv_{los} . Note that the relationship between d_{proj} and Δv_{los} is not strictly inverse; this is because the relative velocity vector is not parallel to the separation vector.

Figure 4 shows the constraints for the five LOS coded by color. For clarity, the figure shows the central 68% confidence interval (CI) rather than multiple individually tailored HPDCI. The first two panels show that the constraints on TSP and v_{\max} become less accurate

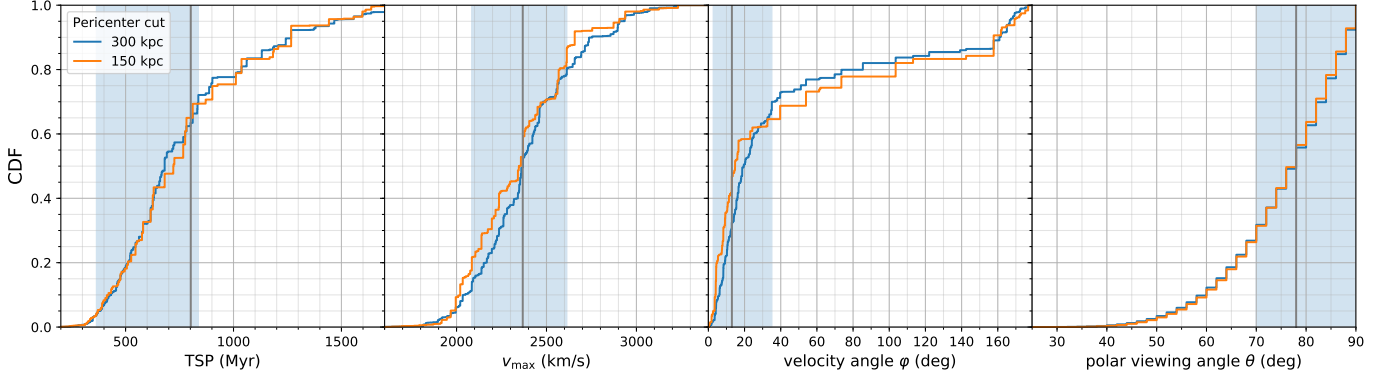


Figure 3. CDFs of dynamical parameters inferred from analogs of System A, with blue curves for all analogs passing the initial 300 kpc cut on pericenter distance, and orange for the subset passing a stricter cut of 150 kpc. The similarity of the curves demonstrates that dynamical parameters can be inferred without prior knowledge of the pericenter distance. The true values (gray lines) are in all cases within the 68% HPDCI (shaded regions) and also close to where the CDF crosses 0.5, which marks the median (likelihood-weighted) analog value. In most panels, each step in the CDF represents the contribution of one analog. In the θ panel, the 2° steps reflect the sampling of lines of sight.

Observer	LOS	θ (deg)	d_{proj} (Mpc)	Δv_{los} (km/s)
1	(1, 0, 0)	56	0.845	56
2	(0, 1, 0)	78	0.999	164
3	(0, 0, 1)	37	0.611	342
4	(1, 0, 1)	80	1.006	24
5	(1, 0, -1)	15	0.272	508

Table 1. Lines of sight of mock observers of System A.

Observer	LOS	θ (deg)	d_{proj} (Mpc)	Δv_{los} (km/s)
1	(1, 0, 0)	35	0.238	1052
2	(0, 1, 0)	72	0.394	1086
3	(0, 0, 1)	61	0.364	874
4	(1, 0, 1)	76	0.403	126
5	(1, 0, -1)	23	0.163	1362
6	(0.82, 0, 1)	82	0.411	9

Table 2. Lines of sight of mock observers of System B.

as the separation vector approaches the LOS ($\theta = 15^\circ$ for Observer 5 and 37° for Observer 3). Nevertheless, the constraints are still workable for Observer 3: the true v_{max} is well within the 68% CI and the true TSP is well within the 90% CI. The third panel shows that the φ inference is stable across the various LOS. The fourth panel is the only panel in which the true value depends on the LOS, and it shows that the θ CDF does not change as much as we would like in response to real changes in the viewing angle. This is because System A has a low $v_{3D}(t_{\text{obs}})$, which is only 3.4 times the observational uncertainty. Hence even the extreme $\theta = 0$ and $\theta = 90^\circ$ models offer predictions for Δv_{los} that conflict only mildly, which limits the ability to distinguish models. As a result, the θ CDF hews closely to that predicted for random observers in the absence of data. This causes Observers 3 and 5 to place the separation vector too close to the plane of the sky, thus underestimating the current 3-D separation given their d_{proj} . This in turn underestimates TSP, the time required to reach that 3-D separation.

We now contrast this with System B, which has $v_{3D}(t_{\text{obs}}) = 1746$ km/s, slightly above the snapshot 74 average of 1437 km/s, in part because it is observed only 215 Myr after pericenter. Table 2 lists the data for the

same five mock observers plus a sixth observer tailored to produce very low Δv_{los} ; Figure 5 shows the inferred CDFs. With System B the true values are more consistently well within the central 68% CI. Furthermore, inferences on TSP, v_{max} , and φ are much more stable across the various LOS, while the inference on θ is much more responsive to the LOS. Still, θ tends to be overestimated when its true value is low, and underestimated when its true value is high. This is a feature of Bayesian inference: estimates are correct on average for an ensemble of observers, but not for selected observers atypical of the prior distribution.

In practice, biases as large as that of Observer 5 on System A will be exceedingly rare: only 3.4% of random observers have $\theta \leq 15^\circ$, and such observers will not identify the system as bimodal to begin with due to their small d_{proj} and small Δv_{los} . The bias also fades for systems with more typical $v_{3D}(t_{\text{obs}})$: compare the moderate TSP bias of System A's Observer 3 ($\theta = 37^\circ$) with the negligible TSP bias of System B's Observer 5 ($\theta = 23^\circ$). A real-life example similar to the low- θ observers of System B is RXC J1314.4-2515, which has Δv_{los} above 1000 km/s and for which WCN found (and we confirm) $\theta \approx 45^\circ$. This supports the contention that

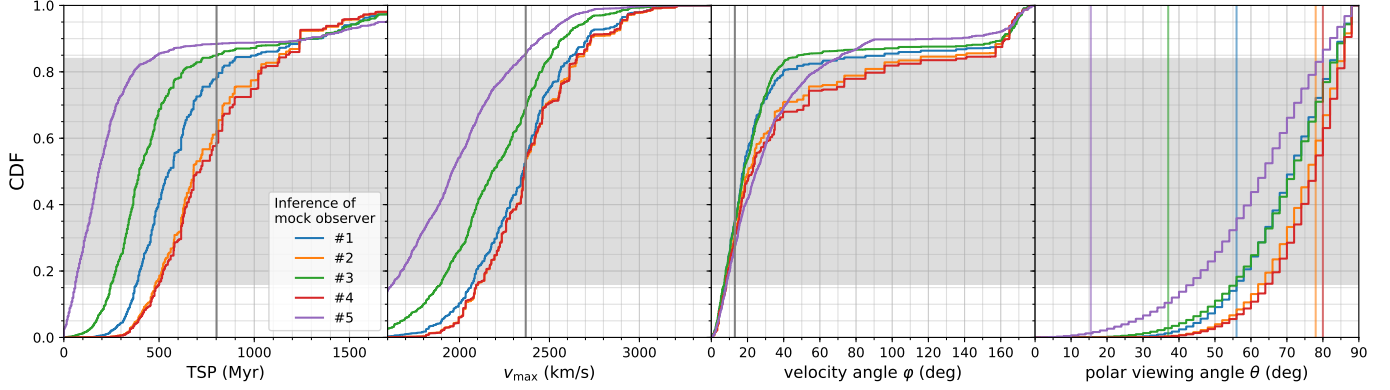


Figure 4. CDFs for dynamical parameters from analogs of System A, for the five different lines of sight and mock observables listed in Table 1. The true values (vertical gray lines) are generally within the central 68% CI (shaded regions), but Observers 3 and 5 underestimate TSP and overestimate θ due to the combination of an atypical system with atypical viewing angles as explained in the text.

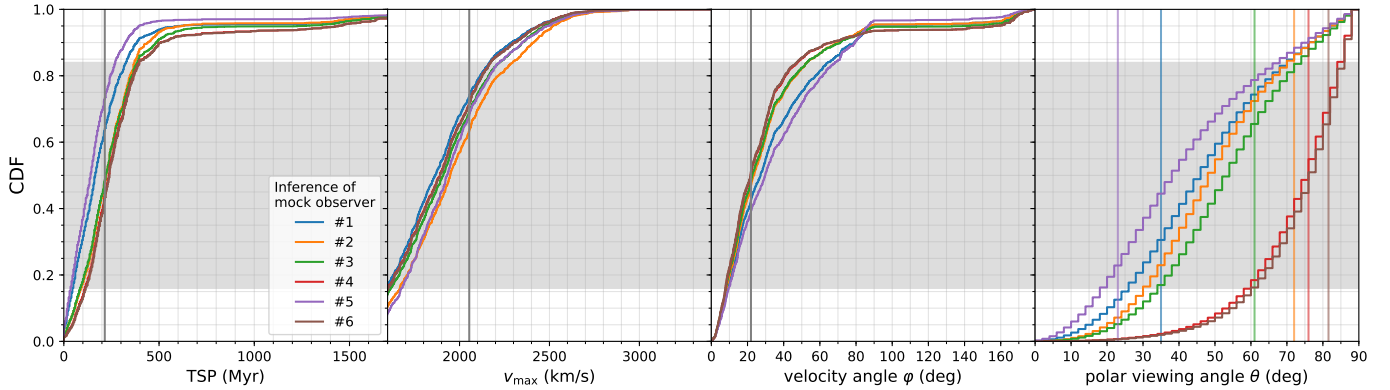


Figure 5. CDFs for dynamical parameters from analogs of System B, for the six lines of sight listed in Table 2. The true values (vertical gray lines) are all well within the central 68% CI (shaded regions).

the θ inference responds to the data where possible while staying closer to a random-observer distribution where it must.

The larger pattern here is, for lack of a better term, regression to the mean. The mean $v_{3D}(t_{\text{obs}})$ of systems in snapshot 74 is 1437 km/s, and System A is in the bottom 2% of systems in this regard. Hence an inference using all systems will necessarily pull the model $v_{3D}(t_{\text{obs}})$ upward *in this case*, leading to an upward bias in θ (to account for the small observed Δv_{los}) which causes a downward bias in the 3-D separation and hence in TSP. However, these effects will reverse for systems with unusually high $v_{3D}(t_{\text{obs}})$ so this is not a bias *per se* but simply the application of cosmologically motivated priors.

3. RESULTS

This section begins by contrasting two clusters in detail to highlight the interpretation of the figures and to point out some trends. Then, we show results for each

cluster in the Golovich et al. (2018) gold sample but with less commentary on each cluster.

3.1. An Illustrative Pair of Systems: ZwCl 0008.8+5215 and MACS J0025.4-1222

We first look at two systems in detail to illustrate what can be learned from the analogs. We choose ZwCl 0008.8+5215 (hereafter ZwCl 0008) and MACS J0025.4-1222 (hereafter MACS J0025) because they are similar in some respects ($\Delta v_{\text{los}} \approx 100$ km/s and similar masses) while differing in d_{proj} (1057 kpc for the former, but only 541 kpc for the latter). They also differ in redshift, with $z = 0.10$ and 0.59 respectively. The values for ZwCl 0008 and MACS J0025 in Table 3 are adopted from Golovich et al. (2018) and Bradač et al. (2008) respectively, with their angular separation values converted to physical using our adopted cosmology. Table 3 lists the values used for all clusters in this paper.

Figures 6 and 7 show the 3-D separation versus time for analogs of ZwCl 0008 and MACS J0025 respectively, with opacity encoding the likelihood of that ana-

Cluster	z	$M_1(10^{14}M_\odot)$	$M_2(10^{14}M_\odot)$	$d_{\text{proj}}(\text{Mpc})$	$\Delta v_r(\text{km/s})$
Merging Cluster Collaboration Gold Sample ^a					
Abell 1240 ^b	0.19	4.19 (0.99)	4.58 (1.40)	1.020 (0.201)	395 (230)
Abell 3411 ^b	0.16	9.0 (5.0)	7.0 (5.0)	1.286 (0.173)	141 (195)
CIZA J2242.8+5301 ^c	0.19	11.0 (3.7)	9.8 (3.8)	1.203 (0.194)	385 (299)
MACS J1149.5+2223 ^d	0.54	8.35 (1.3)	5.45 (3.4)	0.972 (0.394)	228 (281)
MACS J1752.0+4440 ^b	0.36	13.22 (3.14)	12.04 (2.59)	1.177 (0.314)	136 (186)
RXC J1314.4-2515 ^b	0.25	6.07 (1.8)	7.17 (2.8)	0.571 (0.239)	1498 (293)
ZwCl 0008.8+5215 ^e	0.10	5.7 (2.8)	1.2 (1.4)	1.057 (0.119)	110 (155)
ZwCl 1856.8+6616 ^b	0.30	9.66 (4.06)	7.6 (4.05)	0.955 (0.278)	227 (317)
Other Clusters					
MACS J0025.4-1222 ^f	0.59	2.5 (1.7)	2.6 (1.4)	0.541 (0.102)	100 (80)
DLSCl J0916.2+2951 ^g	0.53	3.1 (1.2)	1.7 (2.0)	1.030 (0.144)	670 (330)
1E 0657-558 ^h	0.30	15.0 (1.5)	1.5 (0.15)	0.742 (0.021)	616 (62)

Table 3. Observed values used for each cluster, with uncertainties in parentheses.

^aGolovich et al. (2017b, 2018)

^bWe modify the dynamical mass adopted by Wittman et al. (2018a) as explained in §3.2.

^cJee et al. (2014); Dawson et al. (2014)

^dGolovich et al. (2016); we modify their dynamical mass as explained in §3.2.

^eGolovich et al. (2017a)

^fBradač et al. (2008)

^gDawson (2013); Dawson et al. (2011)

^hDawson (2013); Barrena et al. (2002); Bradač et al. (2006)

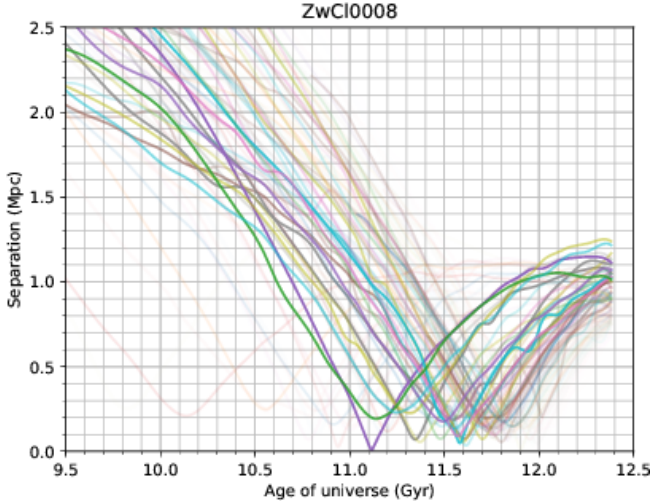


Figure 6. Physical separation versus time for analogs of ZwCl 0008.8+5215. The opacity is proportional to the likelihood of the observed data given the analog, and colors are cycled to better distinguish individual analogs.

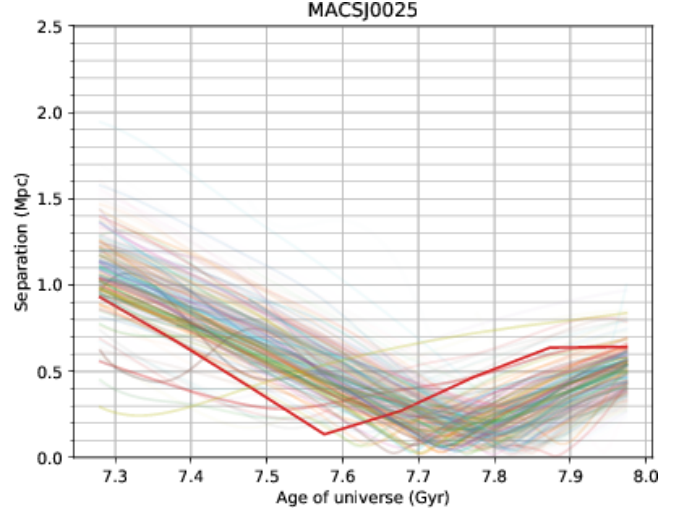


Figure 7. Physical separation versus time for analogs of MACS J0025.4-1222. The opacity is proportional to the likelihood of the observed data given the analog, and colors are cycled to better distinguish individual analogs.

log matching the observables in the final snapshot shown (which is the time of observation). The small minority of trajectories that exhibit ringing from the interpolation still have accurate pericenter distances and times

as explained in §2. Note that the two figures share a common separation scale but not a time scale. This is because ZwCl 0008 analogs are observed at a later snapshot, hence can be traced further back in time. The

MACS J0025 trajectories are shown back to the start of dense time sampling in the BigMDPL database, 7.21 Gyr since the Big Bang, which is only 0.7 Gyr before the time of observation. ZwCl 0008 analogs, in contrast, can be traced many Gyr back (for clarity the figure truncates at 3 Gyr before observation).

The next most salient difference between Figures 6 and 7 is that ZwCl 0008 analogs seem to be falling from greater distances and rebounding to greater distances by the time of observation. The larger infall distance is mostly an artifact of tracing ZwCl 0008 analogs further back in time, while the larger separation at the time of observation is driven by the larger observed projected separation. There *are* some trajectories in Figure 7 with larger separations at the time of observation, but their transparency indicates they are poor matches to the observations. To some extent this is because their 3-D separations substantially exceed the observed d_{proj} of 541 kpc in MACS J0025. This alone is not enough to rule out such analogs, because projection effects can always reduce a large 3-D separation to a small d_{proj} . However, by placing the separation vector more parallel to the line of sight, most such models will predict a large Δv_{los} that yields conflicts with the low value observed for MACS J0025.

This description of the inner workings is supported by the viewing angle constraints in Figure 8. The constraints for the two systems are similar: $\theta > 63^\circ$ (61°) for ZwCl 0008 (MACS J0025) at 90% confidence, or 73° (73°) at 68% confidence. In other words, the viewing angles necessary to reduce d_{proj} to, say, half the 3-D separation are ruled out, and this can be attributed largely to the low observed Δv_{los} . Readers may note that all viewing angles are possible, even with low observed Δv_{los} , if the 3-D relative velocity is low, i.e. the system is observed near turnaround. Nevertheless, Figure 8 implies that line-of-sight configurations in BigMDPL fail to satisfy all the constraints simultaneously, at least for these two observed systems.

There is more to learn from Figures 6 and 7. In both figures, note how analogs with larger current separation tend to have larger TSP (which can be read off by tracing a trajectory leftward from the right edge and locating the minimum). For ZwCl 0008, analogs with large current separations are favored due to the large d_{proj} , and their pericenters occurred ~ 800 Myr ago, albeit with a wide range. Analogs to MACS J0025, in contrast, are scattered across a much smaller and more recent range of TSP.

Yet another dynamical feature implicit in Figures 6 and 7 is the fraction of analogs that are returning after first apocenter (as opposed to still outbound toward first

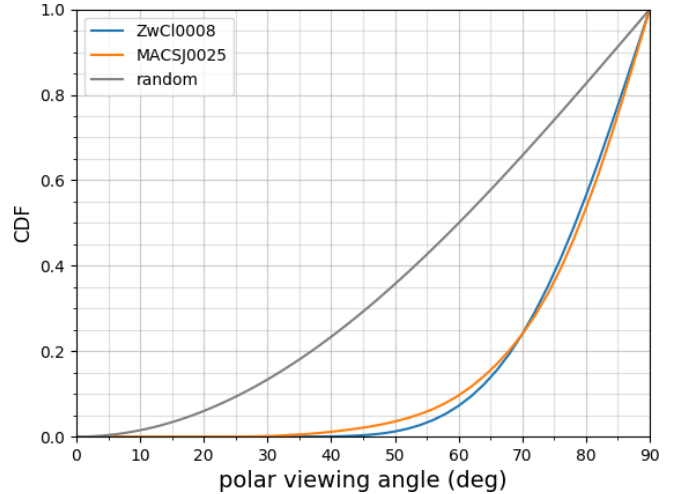


Figure 8. Viewing angle constraints for ZwCl 0008.8+5215 and MACS J0025.4-1222. Here, the convention is that a viewing angle of 90° corresponds to a separation vector in the plane of the sky. The gray curve shows the expected CDF for random viewing angles.

apocenter). For ZwCl 0008, a nonnegligible minority of trajectories fit this description, but for MACS J0025 none do. (The opaque red trajectory is close to apocenter, but in the last snapshot shown it has a velocity vector consistent with outbound, and a separation that increased 5 kpc from the prior snapshot.) Analogs in the returning phase have substantially more TSP than those in the outbound phase, so when they are consistent with observations they can substantially increase the average TSP. In the case of MACS J0025, the lack of returning analogs may be related to its higher redshift of observation—there may not be enough cosmic time for subclusters of the appropriate mass to form, pass through pericenter and then apocenter, and then return to the observed d_{proj} . A strength of the analog method over staged simulations (in which two smooth cluster profiles are set up, then collided) is that this cosmological context is naturally taken into account.

We now present quantitative estimates of the three dynamical quantities TSP, v_{max} , and φ , weighted by analog likelihood. Figure 9 focuses on ZwCl 0008, with likelihoods in the upper panels and CDFs in the lower panels. From left to right the panels show TSP, v_{max} , and φ . Figure 10 echoes this arrangement for MACS J0025.

We first verify that the results are robust to uncertainty in the pericenter distance. Smaller pericenter distance corresponds to a more plunging trajectory, which is more likely to strip gas and presumably to reach a higher speed. Although the gas morphologies in our observed sample indicate close pericenters, we do not have

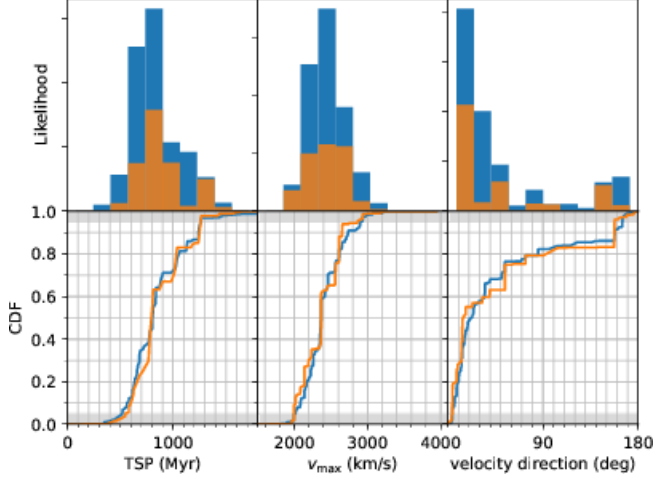


Figure 9. Likelihoods (top row) and CDFs (bottom row) for time since pericenter (left column), v_{\max} (middle column), and velocity angle φ (right column) for ZwCl 0008.8+5215. Blue indicates all analogs, and orange indicates the subset with pericenter distance < 150 kpc. The velocity angle ranges from zero for radially outbound to 180° for radially inbound.

quantitative priors so we plot results for all analogs in blue, and for the subset with pericenter distance < 150 kpc in orange. This is potentially an informative cut because the orange subset includes the most likely pericenter distance for ZwCl 0008 based on comparison of hydrodynamic simulations with X-ray observations Molnar & Broadhurst (2018): 143.5 ± 6.5 kpc (S. Molnar, private communication). Hence the agreement between this subset and all analogs (up to 300 kpc, our initial selection criterion) indicates that such specialized knowledge of the pericenter distance is unnecessary, at least for TSP and v_{\max} . The φ distribution for MACS J0025 is somewhat sensitive to the pericenter cut, but if the primary use of φ is to separate models into outbound ($\varphi < 90^\circ$) and returning ($\varphi > 90^\circ$) then the impact of this cut is negligible.

Because the 150 kpc cut on pericenter distance does not sway the results but does reduce the number of analogs, we use only the initial 300 kpc selection criterion. The impact parameter is a related quantity more commonly quoted by simulators, defined at early times (large separations) as the component of the separation vector perpendicular to the velocity vector. As a rule of thumb, the impact parameter is $\gtrsim 3$ times larger than the pericenter distance (Zhang et al. 2016). Hence our pericenter cut allows impact parameters of $\gtrsim 1$ Mpc, which easily encompasses the range suggested by hydrodynamic simulations of the systems we consider.

With this final selection criterion established, we can read confidence intervals (CI) off Figures 9 and 10. We

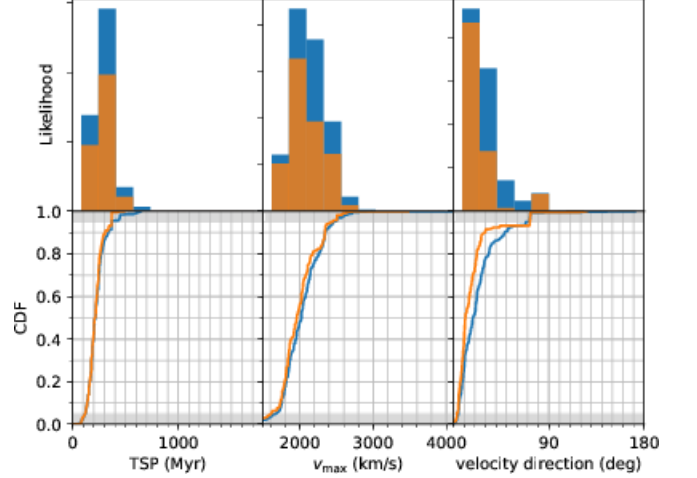


Figure 10. As for Figure 9, but for MACS J0025.4-1222.

find that $616 < \text{TSP} < 1130$ Myr for ZwCl 0008, and $152 < \text{TSP} < 288$ Myr for MACS J0025, at 68% confidence. This confirms the qualitative impression from Figures 6 and 7 that TSP must be greater for ZwCl 0008. Regarding v_{\max} , we find $2139 < v_{\max} < 2653$ km/s at 68% confidence for ZwCl 0008 and $1794 < v_{\max} < 2315$ km/s for MACS J0025. In other words ZwCl 0008 is likely the faster merger, but the ranges do overlap.

Turning to the rightmost columns of Figures 9 and 10, we find that both systems are likely to be outbound ($\varphi < 90^\circ$), at 82% confidence for ZwCl 0008 and 99.6% confidence for MACS J0025. The strong preference for outbound systems is striking, given that every outbound system at a given separation eventually becomes a returning system at the same separation. Due to dissipation, however, the speed when returning at the same separation must be lower. This effect may account for the power of the analogs to discriminate between outbound and returning phases. To test this contention we ran hypothetical versions of ZwCl 0008 with Δv_{los} successively incremented by 100 km/s: the confidence that the system is outbound increased by about 1% for each increment. Hence, the observed relative speed does affect the outbound/returning inference, but only slightly.

The redshift of observation also matters. As mentioned above, at higher redshifts there may not be enough cosmic time for subclusters of the appropriate mass to form, pass through pericenter and then apocenter, and then return to the observed d_{proj} . We tested this by placing the ZwCl 0008 observations at a redshift matching MACS J0025 ($z = 0.59$ rather than 0.10); the confidence in the outbound model jumps up to 95%. For small perturbations in redshift, however, this effect can be obscured by variations in the analog systems selected. (This is not a source of noise when perturbing

Δv_{los} because the same analog systems are used, albeit with perturbed likelihoods.)

In this paper we use φ as a binary outbound/returning indicator, but it may also probe orbital eccentricity as follows. Purely radial orbits will cause the likelihood peak at $\varphi = 0$ to be quite sharp, whereas the inclusion of eccentric orbits will broaden this peak. This is closely related to the question of pericenter distance, which as discussed above may require extending this method to include hydrodynamical simulations.

Comparison with staged hydrodynamic simulations of ZwCl 0008. (Molnar & Broadhurst 2018, hereafter MB18) recently performed a suite of simulations of this system. For a consistent comparison, we rerun the analog method with the modestly higher masses (7 and $5 \times 10^{14} M_{\odot}$) and modestly lower d_{proj} they adopted. The two methods agree that the system is outbound, but the hydrodynamics support this conclusion at high confidence while the analog method yields only 85% confidence. For a consistent comparison with their results we consider only outbound analogs in the following:

- For v_{max} we find a 68% (90%) CI of 2020–2561 (1829–2836) km/s. This is substantially lower than the MB18 value of 3515 km/s, which corresponds to our 99.9999% confidence upper limit. It is possible that the analog speeds are underestimated by more than the 100–200 km/s we have associated with halo particle misidentification. It is also possible that substructure and large-scale structure, which are missing from the staged simulations, prevent v_{max} from reaching the high values seen in staged simulations. To further explore this issue, it will be instructive to apply the analog method to a cosmological simulation with hydrodynamics.
- For TSP we find a 68% (90%) CI of 313–736 (205–990) Myr, both encompassing the MB18 value of 428 Myr. Their value is slightly lower than the center of our range, which is likely related to their higher speed.
- Our viewing angle results are consistent. We find the separation vector is ≥ 73 (≥ 61) degrees from the line of sight at 68% (90%) confidence, while MB18 find that 61° best matches the X-ray morphology.

Note that confidence intervals are not given by MB18 because hydrodynamic simulations are expensive—after doing simulations that bracket a range of parameters to find the best fit, it is infeasible to do many more with slightly perturbed values to support confidence intervals.

A possible further development would be to combine the analog and hydro methods by hydrodynamically resimulating a representative suite of analogs.

3.2. Merging Cluster Collaboration Gold Sample

Golovich et al. (2018) examined a sample of 29 radio-selected merging clusters, including analog viewing angle constraints, and identified a gold subsample of eight cleanly bimodal systems. These are listed in the first block of Table 3. For some clusters noted, only dynamical masses are available but these are biased high in a merger by a factor of two or more (Pinkney et al. 1996; Takizawa et al. 2010). Mass overestimates trigger two difficulties with the analog method. First, in *any* type of dynamical inference, the timescales will be biased low, and the pericenter speeds biased high, because higher masses are associated with greater accelerations from the time of pericenter to the time of observation. However, times and speeds depend sublinearly on the mass (\sqrt{M} dependence for point masses) so this does not necessarily result in a large bias. The more difficult issue arises when the nominal masses are very high *and* have very small nominal uncertainties: few analogs will be found and the single highest-mass analog will dominate the likelihood. This problem is particularly acute for MACS J1149.5+2223 and A3411, with nominal dynamical masses of 37.6 and $32 \times 10^{14} M_{\odot}$ respectively, nominally ≈ 10 times the uncertainty.

We stress that for systems with high *lensing* masses (unlikely to be biased high in a merger) the proper way to find more analogs is to simulate a larger volume. Dynamical masses, however, must be debiased before searching for analogs. We take guidance from studies of the two systems mentioned above. First, Applegate et al. (2014) did a weak lensing study of all mass within 1.5 Mpc of MACS J1149.5+2223. This was done before MACS J1149.5+2223 was recognized to be bimodal, but the 1.5 Mpc radius includes both subclusters. They found $14 \times 10^{14} M_{\odot}$, almost exactly half the dynamical mass and in line with the general bias studies of Pinkney et al. (1996) and Takizawa et al. (2010). Second, a recent X-ray analysis of A3411 (Andrade-Santos *et al.*, submitted) finds $M_{500, Y_X} = 7.1 \times 10^{14} M_{\odot}$, which extrapolates to a total system mass $M_{\text{vir}} \approx M_{200} \approx 10^{15} M_{\odot}$. This is somewhat less than half the total dynamical mass, again in line with the general bias studies cited. The dynamical mass estimates do help apportion the total mass into subcluster masses, because the bias should be similar for both subclusters. Hence, where subcluster lensing masses are unavailable we use half the subcluster dynamical mass, retaining the nominal uncertainties.

Figure 11 shows the TSP constraints, in the form of CDFs, for these eight systems. This provides a clear impression of how to rank the systems from youngest to oldest. To quantify this we define the median analog TSP for a system as the TSP at which that system’s CDF crosses 0.5. RXC J1314.4-2515 is the youngest system with a median analog TSP of 206 Myr. (For comparison, the median analog TSP for MACS J0025, the younger system in §3.1, is 216 Myr.) This is followed by MACS J1149.5+2223 at 256 Myr, then a group of three (A1240, MACS J1752.0+4440, and ZwCl 1856.8+6616) at 400–450 Myr, then CIZA J2242.8+5301 at 608 Myr. Finally, the oldest two systems, at 750–800 Myr, are A3411 and ZwCl 0008.

The individual rankings cannot be established at high confidence because the CDFs overlap, but there is a clear distinction between young, middle-aged, and old. For example, the 68% CI for RXC J1314.4-2515 (90–327 Myr) barely overlaps that of the middle-aged system A1240 (316–946 Myr). These distinctions will become even clearer in cases where prior information can rule out either the outbound or returning phase, as follows. The returning models constitute the long tail toward high TSP, which typically occupies the top 5–20% of the CDF. This is very clear in the case of RXC J1314.4-2515, where the last 5% of the analog likelihood is ≈ 1.5 Gyr older than the first 95%; in other words, it is seen soon after first pericenter or soon before second pericenter, but not in between. In the returning model, the shock would have traveled very far out and would likely be undetectable, but in fact it is detectable and close to the subclusters (Venturi et al. 2013; Mazzotta et al. 2011). This may justify use of outbound analogs only; this has only a minor effect on the median age but would narrow the 95% and 99% CI considerably. Another example is A3411, where a few returning analogs have a high likelihood, yielding the vertical line segments at high TSP in Figure 11. If these could be ruled out on the basis of X-ray morphology (Andrade-Santos *et al.* in preparation), much stricter upper limits could be placed on TSP even as the median analog TSP would fall only modestly, from 755 Myr to 696 Myr.

Figure 12 shows the v_{\max} CDFs. The two illustrative systems considered in §3.1 would both be considered slow in this context: MACS J0025 was found to be about 350 km/s slower than ZwCl 0008, which is seen here in the slower half of the gold sample. The median analog v_{\max} ranges from 2254 km/s for A1240 to 2790 km/s for MACS J1752.0+4440. This is a small range compared to the ≈ 900 km/s spanned by the 90% CI of a typical system; in other words, the differences in v_{\max} from system to system are not highly significant.

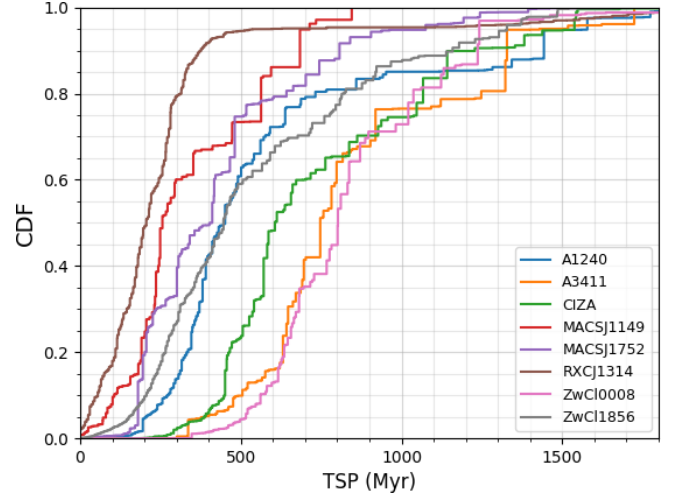


Figure 11. Cumulative distribution functions for time since pericenter for the gold sample defined by Golovich et al. (2018).

Nevertheless, the higher-mass systems do tend to have higher v_{\max} as one would expect from dynamics. There is no apparent relationship between the TSP ordering seen in Figure 11 and the v_{\max} ordering seen here.

Note that RXC J1314.4-2515 has a remarkably high observed Δv_{los} (1498 km/s) yet is unremarkable, even a bit low, in terms of v_{\max} . Part of the explanation lies in projection effects; we agree with WCN18 and Golovich et al. (2018) that the most likely viewing angle is around 45° , which exposes a larger fraction of its current 3-D velocity than do other systems. We quantify this by tabulating the median analog 3-D velocity at the time of observation. We find 1827 km/s, which is still roughly a factor of two higher than for most other systems considered here. Hence projection cannot be the only factor behind the high observed Δv_{los} . The low TSP provides a second factor: this system has had less time to slow down since pericenter. This provides a lesson that the observed Δv_{los} , and even its deprojection, should not be used as a proxy for merger speed.

Figure 13 shows the φ CDFs for the same sample. The system most likely to be in the returning phase ($\varphi > 90^\circ$) is A3411, but even here the likelihood of being outbound is great (66%). CIZA J2242.8+5301 has a 72% likelihood, and all other systems have 82% or greater likelihood, of being in the outbound phase. Higher-redshift systems tend to be more likely outbound compared to lower-redshift systems, which supports the discussion of this effect in §3.1. As discussed above, X-ray morphology or shock position may be more powerful ways to determine the phase; if so, restricting analogs to the correct phase will provide tighter constraints on other quantities, especially TSP.

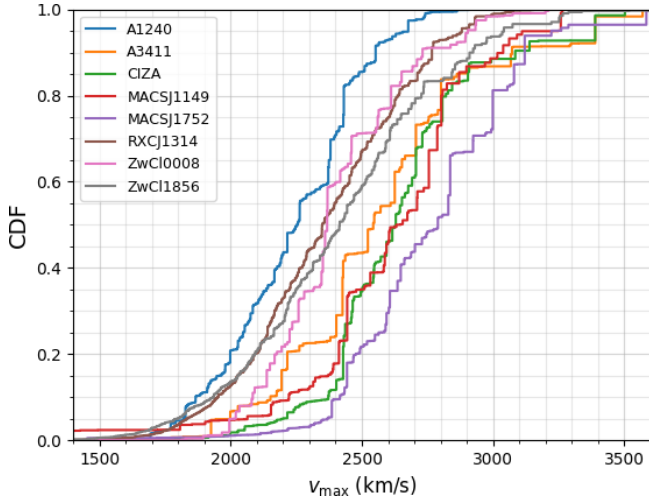


Figure 12. Cumulative distribution functions for v_{\max} for the gold sample defined by Golovich et al. (2018).

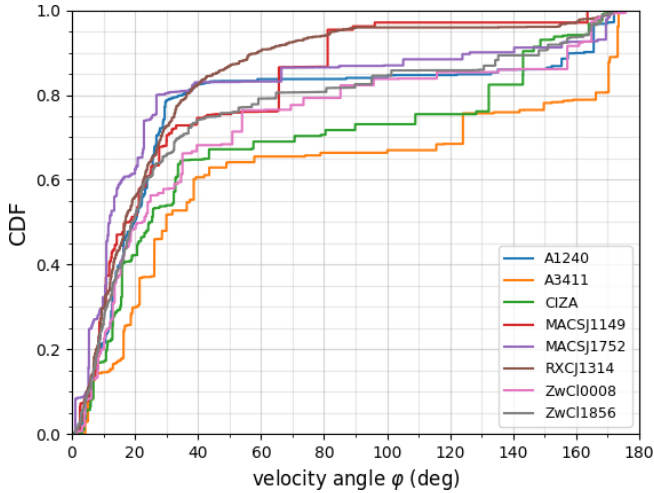


Figure 13. Cumulative distribution functions for φ for the gold sample defined by Golovich et al. (2018).

Comparison with staged hydrodynamic simulations of ClZA J2242.8+5301. Molnar & Broadhurst (2017) recently performed a suite of simulations of this system. For a consistent comparison, we rerun the analog method with their lower subcluster mass estimates (5.0 and $3.9 \times 10^{14} M_{\odot}$). We agree (with 76% confidence) that the system is outbound. We adopt this conclusion and consider only outbound analogs in the following:

- For v_{\max} we find a 68% (90%) CI of 2029–2661 (1916–2746) km/s. Molnar & Broadhurst (2017) do not list their maximum speed, but it must be substantially higher than this because their model already has a relative speed of 2500 km/s when the two virial radii first touch (fully 700 km/s faster than they found for ZwCl 0008). This reinforces

the notion that the analogs may be underestimating the maximum speed by more than the 100–200 km/s described in §2, and/or that staged simulations may overestimate the maximum speed because they lack substructure and large-scale structure.

- For TSP we find a 68% (90%) CI of 425–767 (291–1052) Myr, consistent with the Molnar & Broadhurst (2017) value of 0.4 Gyr. Their value is definitely lower than the center of our range, which is again likely related to their higher speed.
- Molnar & Broadhurst (2017) suggest that at the time of observation the separation vector is 75° from the line of sight. We agree, with 68% (90%) confidence lower limits of 70 (59) degrees.

4. COMPARISON TO MCMAC

We now compare our results to those of Dawson (2013), hereafter D13, who analyzed the Bullet cluster (1E 0657-558) and the older and slower Musketball cluster (DLSC J0916.2+2951) with MCMAC. We adopt the Δv_{los} and mass values used by D13, which came from observations by Barrena et al. (2002) and Bradač et al. (2006) for the Bullet, and by Dawson et al. (2011) for the Musketball. D13 drew d_{proj} values from these sources as well; we convert those to angular values using his assumed cosmology, and then back to kpc using the BigMDPL cosmology, which increases the physical values by about 3%. We display trajectories of the analogs in Figure 14 and dynamical inferences in Figure 15.

We begin with the Musketball. We find a 68% CI of 333–590 Myr for TSP, compared to 700–2400 Myr found by D13. We attribute this to the effect explained in §1: because the MCMAC model examines only radial trajectories, it is forced to explain nonzero Δv_{los} by reducing θ from its *a priori* most likely value of 90° . In contrast, in BigMDPL analogs the relative velocity vector usually has a component perpendicular to the separation vector, which readily allows $\theta = 90^{\circ}$ models (i.e. the separation vector is in the plane of the sky) unless the observed Δv_{los} is more than a few hundred km/s. The Musketball Δv_{los} of 630 ± 330 km/s is enough to broaden the likelihood peak away from $\theta = 90^{\circ}$, yielding a plateau across the range 78 – 90° . This contrasts with the D13 estimate that $\theta \approx 48^{\circ}$ is most likely. (In terms of 68% CI, we find $\theta \geq 65^{\circ}$, whereas D13 found 23 – 62° .) Hence MCMAC infers a substantially larger 3-D separation at the time of observation, which in turn requires more TSP to reach that separation.

The two methods agree on v_{\max} : we find a 68% CI of 2178–2582 km/s, while D13 found 2000–2500 km/s.

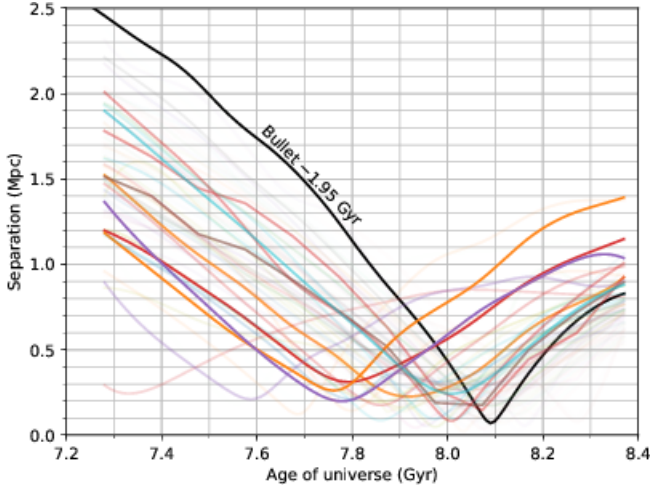


Figure 14. Colored curves show physical separation versus time for analogs of the Musketball cluster, with opacity indicating the likelihood. The black curve is the dominant analog for the Bullet cluster, shifted in time so the observed states (the ends of the curves) can be compared.

(As noted in §2, the maximum velocity recorded in the BigMDPL snapshots, which we quote here, may underestimate the maximum simulated velocity by 100–200 km/s.)

Analogues provide two additional quantities that cannot be provided by MCMAC. First, the analytical model in MCMAC can make no distinction between outbound and returning phases. The D13 TSP we quoted assumes the outbound phase, but D13 provided a second TSP that assumes the returning phase: 2.0–7.2 Gyr. Our analogs favor the outbound phase at 97% confidence. (The few returning analogs we do find have $\text{TSP} \approx 0.9$ Gyr, indicating that our analogs have shorter periods than in the D13 calculation.) Second, MCMAC assumes zero pericenter distance, but we are able to extract the pericenter distance of the analogs. We find a median analog pericenter distance of 180 kpc, with negligible probability that the pericenter distance is less than 20 kpc. This is a case where improved constraints on pericenter distance, perhaps from hydrodynamic simulations, could improve the analog constraints. The Musketball does have analogs with large pericenter distances (180–280 kpc) and these favor $\text{TSP} \approx 600$ Myr. If these large pericenter distances could be ruled out based on the dissociative X-ray morphology, the TSP estimates would tighten around 350 Myr, near the lower end of our current range. There would be little effect on the v_{max} and outbound/returning estimates in this scenario.

For the Bullet, D13 offers two sets of results: a default set, and one with an additional prior limiting the TSP, which is justified based on the observation of transient X-ray effects such as the shock front and increased X-ray

luminosity (compared to expectations from the lensing mass). This has the effect of reducing the 68% CI for TSP from 0.3–1.1 Gyr to 0.3–0.5 Gyr, assuming the outbound phase. We will compare our results to the latter set of D13 results.

We find that one analog dominates, providing 98.9% of the weight, because the observational uncertainties listed by D13 are quite small. Rather than attempt to give confidence intervals, we focus on this one dominant analog. This analog is consistent with the D13 estimates. Its TSP is 281 Myr, a bit below the D13 68% CI but well within his 95% CI of 0.2–0.6 Gyr. The analog has a v_{max} of 2863 km/s, well within the D13 68% CI of 2600–3300, and a most likely θ of 81° , which is slightly outside the D13 68% CI of $52\text{--}74^\circ$, but understandable on the basis of D13’s radial assumption. The analog also has a pericenter distance of 74 kpc and a current angle of 11° between the velocity and separation vectors.

The next most likely analog carries almost 1% of the weight and is quite similar: $\text{TSP} = 291$ Myr, $v_{\text{max}} = 2871$ km/s, and $\varphi = 10^\circ$, but with a larger pericenter distance of 136 kpc. Providing confidence intervals for the Bullet would require finding additional analogs that can compete with the dominant analog. If the fairly strict uncertainties on observed quantities are correct in this well-observed system, this would in turn require simulating a larger volume. MCMAC, in contrast, is always able to provide smooth formal confidence intervals because analytical models can always be perturbed, while the analog method is limited by the discrete number of available analogs. This weakness of the analog method could potentially be ameliorated by using “genetically modified” simulations (Rey & Pontzen 2018) to produce larger quantities of relevant analogs.

Even a single analog can be viewed from a range of angles, making confidence intervals on θ mathematically possible. The dominant Bullet analog, for example, yields a formal 90% CI of $73\text{--}84^\circ$. Such confidence intervals do not reflect marginalization over a cosmologically motivated range of impact parameters, so we recommend caution in this regard. This dominant analog nevertheless agrees with D13 and WCN18 in putting the separation vector $10\text{--}20^\circ$ from the plane of the sky.

Finally, we note that hydrodynamic simulations of the Bullet cluster (Springel & Farrar 2007) prefer a younger model with TSP of 180 Myr. The observed separation is achieved quickly with $v_{3D}(t_{\text{obs}}) \approx 2700$ km/s, versus our dominant analog with a *maximum* speed of 2863 km/s and a current speed of 1965 km/s. This continues the pattern in which staged hydrodynamic simulations produce higher speeds than our analogs. Further work,

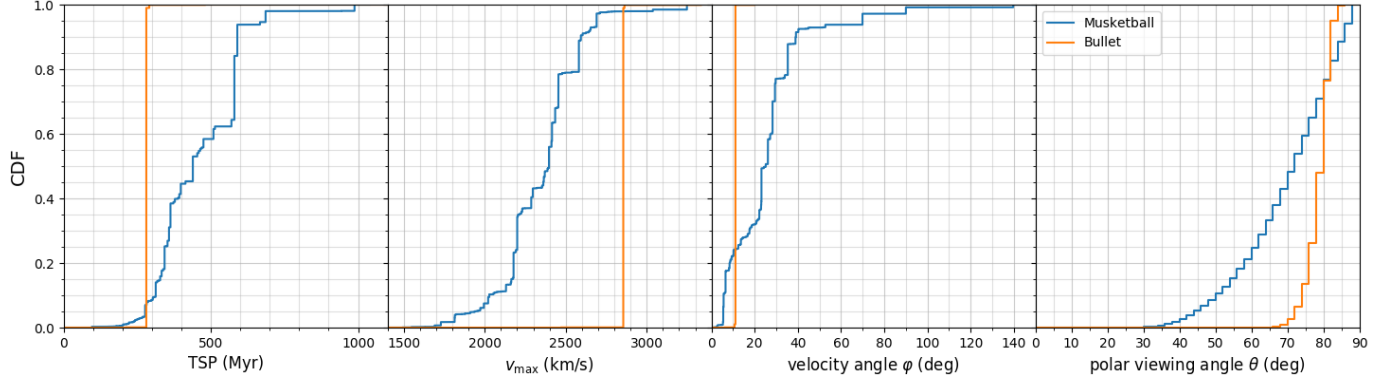


Figure 15. Analog constraints on the properties of the Muskettball are shown in blue. Properties of the single dominant Bullet analog are shown in orange.

perhaps with cosmological hydrodynamical simulations, will be needed to clarify the source of this discrepancy.

5. SUMMARY AND DISCUSSION

We identified analogs of observed merging galaxy clusters in the BigMDPL cosmological n-body simulation based only on subcluster masses, relative line-of-sight speed, and projected separation. We then extracted dynamical properties of the analogs such as time since pericenter, maximum relative speed, and merger phase (outbound or returning) at the time of observation. Table 4 lists highest probability density confidence intervals for TSP and v_{\max} , as well as the percentage confidence that the system is outbound.

Our major results are:

- Although the uncertainties on TSP can be in the hundreds of Myr, the analogs can distinguish between “young” mergers seen 200–280 Myr after pericenter (MACS J1149.5+2223, RXC J1314.4-2515, MACS J0025.4-1222, and the Bullet), intermediate systems at 400–450 Myr (MACS J1752.0+4440, Abell 1240, ZwCl 1856.8+6616, and the Muskettball) and “old” mergers seen 600 Myr (CIZA J2242.8+5301) or even 700–800 Myr (Abell 3411 and ZwCl 0008.8+5215) after pericenter.
- All these systems are more likely to be outbound than returning, but in most cases the returning phase cannot be ruled out at high confidence based on these analog matching criteria alone. Because of this, 95% confidence upper limits on TSP can be up to 1 Gyr older than the central values given above. If, for any given system, one or the other phase can be ruled out on the basis of other information, the limits on TSP for that system will shrink dramatically. This in turn will improve inferences about time-dependent physical processes

such as dark matter displacements (Kim et al. 2017).

- The probability of being in the returning phase increases with the cosmic time of observation. It also increases (albeit weakly) if one lowers the observed line-of-sight relative velocity while keeping the other parameters fixed.
- The maximum speed v_{\max} ranges from about 2000 km/s for MACS J0025.4-1222 to about 2800 km/s for MACS J1752.0+4440 and the Bullet. The v_{\max} estimate depends mostly on the mass used for the analog selection, and not so much on the observed line-of-sight relative velocity. This is an indication that the underlying dynamics are being recovered, independent of viewing angle and time of observation. However, the maximum speed we tabulate in BigMDPL snapshots is underestimated by 100-200 km/s because of difficulties in assigning particles to halos at the time of pass-through.

Regarding the development and applicability of the method, we find:

- The analog method is fast, requiring only seconds of CPU time on a laptop computer per observed system after initial setup. It also naturally incorporates the effects of dynamical friction, substructure, and large-scale structure; and marginalizes over a cosmologically motivated range of impact parameters and trajectories.
- The simulation we use here to demonstrate the method, BigMDPL, has dark matter only. This inclusion of hydrodynamics could affect the results stated above, but this method can easily be applied to bigger and better simulations as they become available.

Cluster	TSP (Myr, 68% CI)	TSP (95% CI)	v_{\max} (km/s, 68%)	v_{\max} (95%)	% outbound
Merging Cluster Collaboration Gold Sample					
Abell 1240	195–577	195–1583	1979–2466	1758–2683	84
Abell 3411	476–971	258–1438	2194–2808	1926–3502	66
CIZA J2242.8+5301	378–937	378–1576	2403–2808	2135–3502	72
MACS J1149.5+2223	181–569	15–734	2391–2888	1903–3264	96
MACS J1752.0+4440	180–491	135–1113	2444–3034	1838–3264	87
RXC J13144.4–2515	100–328	0–627	2018–2653	1786–2934	96
ZwCl 0008.8+5215	516–897	411–1267	2020–2461	1995–2938	81
ZwCl 1856.8+6616	50–627	95–1373	2036–2749	1555–3046	82
Other Clusters					
MACS J0025.4–1222	132–258	71–370	1749–2204	1503–2509	100
DLSCL J0916.2+2951	333–590	267–782	2054–2457	1814–2699	97
1E 0657–558	281 (single analog)		2863 (single analog)		100

Table 4. Inferred dynamical properties of merging clusters.

- For a few observed systems, the method is hampered by lack of analogs. Larger simulation volumes will be welcome, but we also note that lack of analogs can also result from unrealistically small nominal uncertainties on observed quantities. Hence it is important for observers to capture all sources of uncertainty and, ideally, make their full likelihood (or posterior) distributions available.
- Analog selection could likely be improved if analogs were selected from a hydrodynamic simulation based on likelihood of matching the observed X-ray morphology. This would particularly help with constraining the pericenter distance and outbound versus returning phase. In a simplified version of this, we eliminated returning analogs of ZwCl 0008.8+5215 and CIZA J2242.5+2223 based on previously published comparison of staged simulations with the X-ray morphology (Molnar & Broadhurst 2018, 2017). This in turn improved the upper limits on TSP (because returning analogs have such large TSP), which highlights the complementarity of the two methods. Prior knowledge of the pericenter distance is less important for the clusters examined in this paper, but may prove useful for clusters that are far from head-on (e.g. Abell 115; Kim et al. 2019)
- In principle, the shock location—using X-ray or radio observations—could also be included in the analog selection criteria. However, this requires higher resolution simulations than required for gross X-ray morphology, and may be infeasible with cosmological box sizes. One workaround could be to use the basic analog selection technique to identify targets for zoom simulations with

hydrodynamics, which then help refine the analog likelihoods.

- The analogs suggest that all the systems studied here are outbound rather than returning, but no conclusion can be made at high confidence. Thus, the best way to apply the analog method may be to identify the phase based on X-ray morphology or shock position, and use this to inform the analog selection. None of the systems studied here are returning based on these criteria, so studying analogs of known returning systems could be a direction for future work.

To compare with the analytical MCMAC (Dawson 2013) method, we analyzed the same two clusters considered in that paper, using the same inputs. We agree with D13 that the Musketball ((DLSCL J0916.2+2951) is older and slower than the Bullet (1E 0657-558). In more detail:

- We find $v_{\max} \approx 2350$ km/s for the Musketball and $v_{\max} \approx 2850$ km/s for the Bullet, in agreement with D13; however we remind readers that the true numbers must be somewhat higher due to limitations of the BigMDPL halo catalog, and that our Bullet results are based on a single highly dominant analog.
- Our TSP is lower than that of D13, by a factor of a few for the Musketball. This is because our analogs have separation vectors substantially closer to the plane of the sky, hence a smaller current 3-D separation vector which can be reached in less time from pericenter. This in turn stems from the bias identified by WCN18: the assumption of a radial trajectory artificially prohibits plane-of-

sky configurations when (as for most observed systems) Δv_{los} is nonzero. We also find a lower TSP for the Bullet, but here the disagreement is smaller because the two methods agree on the viewing angle.

- In principle the analog method can determine whether a system is outbound or returning, whereas in MCMAC this is a discrete degeneracy. The dominant Bullet analog is outbound and Musketball analogs favor outbound at 97% confidence.

We also compared our results with staged hydrodynamical simulations of ZwCl 0008 (Molnar & Broadhurst 2018) and ClZA J2242.8+5301 (Molnar & Broadhurst 2017). We agree on the merger phase (both systems are outbound rather than returning) and TSP, but disagree on pericenter speed: the staged simulations are $\gtrsim 1000$ km/s faster. This discrepancy may be due to some combination of missing hydrodynamic effects in BigMDPL and missing cosmological effects (substructure, large-scale structure) in the staged simulations. To include all relevant effects, likely analogs should be res-

imulated with hydrodynamics included. Another possibility is that the analog method relies on observed Δv_{los} values that are underestimated; mistakes in assigning galaxies with spectroscopic redshifts to subclusters will always reduce the apparent relative velocity of the subclusters. To investigate this possibility, simulations could be used to generate mock observations of subhalo positions and redshifts, to be analyzed with the same subclustering techniques used by observers.

I thank the anonymous referee and Matthew Self for useful comments, Sandor Molnar for discussions regarding his simulation results, and Will Dawson for the original idea several years ago. This work was supported in part by NSF grant 1518246. The CosmoSim database used in this paper is a service by the Leibniz-Institute for Astrophysics Potsdam (AIP). The MultiDark database was developed in cooperation with the Spanish MultiDark Consolider Project CSD2009-00064. This work also made use of `astropy.cosmology` and Ned Wright’s online cosmology calculator (Wright 2006).

REFERENCES

- Applegate, D. E., von der Linden, A., Kelly, P. L., et al. 2014, *Monthly Notices of the Royal Astronomical Society*, 439, 48
- Barrena, R., Biviano, A., Ramella, M., Falco, E. E., & Seitz, S. 2002, *A&A*, 386, 816
- Behroozi, P. S., Wechsler, R. H., & Wu, H.-Y. 2013, *ApJ*, 762, 109
- Bradač, M., Allen, S. W., Treu, T., et al. 2008, *ApJ*, 687, 959
- Bradač, M., Clowe, D., Gonzalez, A. H., et al. 2006, *ApJ*, 652, 937
- Brunetti, G., & Jones, T. W. 2014, *International Journal of Modern Physics D*, 23, 30007
- Chung, S. M., Gonzalez, A. H., Clowe, D., Markevitch, M., & Zaritsky, D. 2010, *ApJ*, 725, 1536
- Dawson, W. A. 2013, *ApJ*, 772, 131
- Dawson, W. A., Wittman, D., Jee, M., et al. 2011, *ArXiv e-prints*, arXiv:1110.4391
- Dawson, W. A., Jee, M. J., Stroe, A., et al. 2014, *ArXiv e-prints*, arXiv:1410.2893
- Ensslin, T. A., Biermann, P. L., Klein, U., & Kohle, S. 1998, *A&A*, 332, 395
- Feretti, L., Giovannini, G., Govoni, F., & Murgia, M. 2012, *A&A Rv*, 20, 54
- Golovich, N., Dawson, W. A., Wittman, D., et al. 2016, *ApJ*, 831, 110
- Golovich, N., van Weeren, R. J., Dawson, W. A., Jee, M. J., & Wittman, D. 2017a, *ApJ*, 838, 110
- Golovich, N., Dawson, W. A., Wittman, D. M., et al. 2017b, *ArXiv e-prints*, arXiv:1711.01347
- . 2018, *ArXiv e-prints*, arXiv:1806.10619
- Harvey, D., Robertson, A., Massey, R., & McCarthy, I. G. 2018, *ArXiv e-prints*, arXiv:1812.06981
- Jee, M. J., Stroe, A., Dawson, W., et al. 2014, *ArXiv e-prints*, arXiv:1410.2898
- Kahlhoefer, F., Schmidt-Hoberg, K., Frandsen, M. T., & Sarkar, S. 2014, *MNRAS*, 437, 2865
- Kahn, F. D., & Woltjer, L. 1959, *ApJ*, 130, 705
- Kim, M., Jee, M. J., Finner, K., et al. 2019, *ApJ*, 874, 143
- Kim, S. Y., Peter, A. H. G., & Wittman, D. 2017, *MNRAS*, 469, 1414
- Klypin, A., Yepes, G., Gottlöber, S., Prada, F., & Heß, S. 2016, *MNRAS*, 457, 4340
- Ma, C. J., Ebeling, H., Marshall, P., & Schrabback, T. 2010, *MNRAS*, 406, 121
- Mansheim, A. S., Lemaux, B. C., Tomczak, A. R., et al. 2017, *MNRAS*, 469, L20
- Markevitch, M., Gonzalez, A. H., Clowe, D., et al. 2004, *ApJ*, 606, 819

- Mazzotta, P., Bourdin, H., Giacintucci, S., Markevitch, M., & Venturi, T. 2011, *Mem. Soc. Astron. Italiana*, 82, 495
- Miller, N. A., & Owen, F. N. 2003, *AJ*, 125, 2427
- Molnar, S. M., & Broadhurst, T. 2017, *ApJ*, 841, 46
- . 2018, *ApJ*, 862, 112
- Navarro, J. F., Frenk, C. S., & White, S. D. M. 1997, *ApJ*, 490, 493
- Pinkney, J., Roettiger, K., Burns, J. O., & Bird, C. M. 1996, *ApJS*, 104, 1
- Planck Collaboration, Ade, P. A. R., Aghanim, N., et al. 2014, *A&A*, 571, A16
- Randall, S. W., Markevitch, M., Clowe, D., Gonzalez, A. H., & Bradač, M. 2008, *ApJ*, 679, 1173
- Rey, M. P., & Pontzen, A. 2018, *MNRAS*, 474, 45
- Robertson, A., Massey, R., & Eke, V. 2017, *MNRAS*, 465, 569
- Skillman, S. W., Xu, H., Hallman, E. J., et al. 2013, *ApJ*, 765, 21
- Sobral, D., Stroe, A., Dawson, W. A., et al. 2015, *MNRAS*, 450, 630
- Springel, V., & Farrar, G. R. 2007, *MNRAS*, 380, 911
- Stroe, A., Sobral, D., Paulino-Afonso, A., et al. 2017, *MNRAS*, 465, 2916
- Takizawa, M., Nagino, R., & Matsushita, K. 2010, *PASJ*, 62, 951
- Venturi, T., Giacintucci, S., Dallacasa, D., et al. 2013, *A&A*, 551, A24
- Wittman, D., Cornell, B. H., & Nguyen, J. 2018a, *ApJ*, 862, 160
- Wittman, D., Golovich, N., & Dawson, W. A. 2018b, *ApJ*, 869, 104
- Wright, E. L. 2006, *PASP*, 118, 1711
- Zhang, C., Yu, Q., & Lu, Y. 2016, *ApJ*, 820, 85